communications biology

A Nature Portfolio journal

Article

https://doi.org/10.1038/s42003-025-07654-3

Elevated levels of S100A8 and S100A9 exacerbate muscle mitochondrial fragmentation in sepsis-induced muscle atrophy

Dongqin Huang[1,5], Yang Li[2,5], Yuqian Guo[3], Mengcao Weng[4], Hui Ye[3], Yan Zhang[4], Fei Lin[1], Kai Zhang[3,6] ✉ & Xiangming Fang[1,3,6] ✉

Sepsis-induced skeletal muscle atrophy is common in septic patients with the increases risk of mortality and is associated with myocellular mitochondrial dysfunction. Nevertheless, the specific mechanism of sepsis muscle atrophy remains unclear. Here we conducted a clinical retrospective analysis and observed the elevation of skeletal muscle index (ΔSMI) was an independent risk factor for 60-day mortality in septic patients. Moreover, in mouse model of sepsis, the skeletal muscle atrophy was also observed, which was associated with the upregulation of S100a8/a9-mediated mitochondrial dysfunction. Inhibition of S100a8/a9 significantly improved mitochondrial function and alleviated muscle atrophy. Conversely, administration of recombinant S100a8/a9 protein exacerbated mitochondrial energy exhaustion and myocyte atrophy. Mechanistically, S100a8/a9 binding to RAGE induced Drp1 phosphorylation and mitochondrial fragmentation, resulting in muscle atrophy. Additionally, RAGE ablation or administration of Drp1 inhibitor significantly reduced Drp1-mediated mitochondrial fission, improved mitochondrial morphology and function. Our findings indicated the pivotal role of S100a8/a9 in driving the mitochondrial fragmentation in septic muscle atrophy. Targeting S100a8/a9-RAGE-initiated mitochondrial fission might offer a promising therapeutic intervention against septic muscle atrophy.

Sepsis, a life-threatening organ dysfunction triggered by a dysregulated host response to infection, poses a significant threat to global health[1]. Skeletal muscle atrophy is a prevalent consequence of sepsis, with the prevalence of around 40% to 70%[2]. This atrophy is characterized by progressive muscle wasting, weakness, and dysfunction of myofibers[3]. Importantly, sepsis with muscle atrophy is a major risk factor for both in-hospital and post-hospital mortality, affecting millions of survivors and contributing to a higher risk of hospital readmission[4]. It also increases susceptibility to infections and diminishes the quality of life related to physical disability[5]. Studies have investigated the muscle atrophy at certain stages of sepsis, however, the degree of early and sustained loss of muscle tissue in sepsis and its association with the prognosis of septic patients remains unclear, as does the exact mechanism underlying muscle atrophy in septic conditions.

Mitochondrial dysfunction has emerged as a hallmark of sepsis-induced muscle atrophy, disrupting the delicate balance of mitochondrial fusion and fission which is essential for maintaining mitochondrial quality and function[6–8]. This balance is intricately linked to skeletal muscle metabolism and health, influencing muscle mass maintenance and contraction, and energy production and consumption[9–11]. Dynamin-related protein 1 (Drp1) is a key regulator of mitochondrial fission, with its increased phosphorylation at serine 616 ($Drp1^{ser616}$) closely associated with mitochondrial fragmentation[12]. Genetic interventions involving Drp1 have demonstrated therapeutic effects on muscle mass and systemic

[1]Department of Anesthesiology, Guangxi Medical University Cancer Hospital, Nanning, China. [2]Department of Critical Care Medicine, Guangxi Medical University Cancer Hospital, Nanning, China. [3]Department of Anesthesiology, The First Affiliated Hospital, Zhejiang University School of Medicine, Hangzhou, China. [4]Children's Hospital, Zhejiang University School of Medicine, National Clinical Research Center for Child Health, Hangzhou, China. [5]These authors contributed equally: Dongqin Huang, Yang Li. [6]These authors jointly supervised this work: Kai Zhang, Xiangming Fang. ✉e-mail: Kai_zhang@zju.edu.cn; xmfang@zju.edu.cn

metabolism[13,14]. However, the effect of Drp1 in sepsis-induced muscle atrophy is still unclear.

The origin of muscle atrophy in sepsis is attributed to circulating pathogens and cytokines contributing to a cytokine storm[15]. Cytokine storm disrupts cellular signaling pathways, leading to decreased protein synthesis and accelerated protein degradation[16,17]. Various inflammatory molecules, including IL-6, IL-1β, and serum amyloid A1 (SAA1), have been implicated in these processes[18–20]. In particular, preventing cytokine-induced muscle atrophy is considered crucial for improving physical ability. Therefore, it's important to investigate inflammatory molecular targets for prevention or treatment of muscle atrophy in sepsis.

In our current study, we observed that the high skeletal muscle atrophy increased disease severity and 60-day mortality in septic patients. Transcriptome analysis from animal experiments revealed mitochondrial dysfunction in septic muscle atrophy, and S100a8/a9, a notable inflammatory molecule, was identified as a significant contributor to mitochondrial dysfunction by promoting receptor for advanced glycation end products (RAGE)-mediated mitochondrial Drp1 phosphorylation. These findings present a potential therapeutic avenue against septic muscle atrophy.

Results

The high skeletal muscle index (△SMI) is an independent risk factor for 60-day mortality in septic patients

To investigate the impact of skeletal muscle atrophy on sepsis mortality, we conducted a retrospective study from Jan 2020 to Oct 2022, enrolling 86 septic patients based on screening criteria (Fig. 1a). The clinical characteristics of the patients are detailed in Supplementary Table 1. Within the sepsis study cohort, 86 patients were included, comprising 47(54.65%) males and 39(45.35%) females. All patients had a mean age of 66.67 years with range from 22 to 90 years. Within 60 days, 26(30.23%) patients succumbed to sepsis. Through receiver operating characteristic (ROC) curve analysis, we determined an optimal cutoff value of 7.2 cm^2/m^2/30 days for ΔSMI. Among the 86 septic patients, 49 (56.98%) fell into the low ΔSMI cohort, while 37 (43.02%) were classified as high ΔSMI cohort. The 60-day mortality rate in the high ΔSMI cohort was significantly higher than that in the low ΔSMI cohort (log-rank $\chi^2 = 16.720$; $P < 0.001$) (Fig. 1b and Supplementary Table 1).

Two illustrative cases are presented in Fig. 1c, A 71-year-old septic patient who succumbed 40 days after sepsis onset, with a ΔSMI of 15.40 cm^2/m^2/30 days, categorized as high ΔSMI (Fig. 1c (upper CT image)). A 69-year-old septic patient with an extended survival time whose ΔSMI was 0.93 cm^2/m^2/30 days, classified as low ΔSMI (Fig. 1c (lower CT image)). Furthermore, multivariate logistic regression analysis confirmed high ΔSMI (OR = 5.888, 95% CI 2.069–16.752, $P = 0.001$) as an independent risk factor for 60-day mortality, adjusting for age, mechanical ventilation, vasopressor infusions, and MODS (Fig. 1d). Intriguingly, ΔSMI levels exhibited a positive correlation with SOFA scores (R = 0.2557, $P = 0.0175$, Fig. 1e). These findings suggest that high ΔSMI is associated with a more severe condition, establishing it as an independent risk factor for septic mortality.

Skeletal muscle atrophy is associated with mitochondrial dysfunction in septic mouse model

To investigate the pathological changes associated with septic muscle atrophy, we dynamically evaluated skeletal muscle weight, histomorphology, expression of muscle atrophy biomarkers, and muscle strength in a murine septic model induced by cecal ligation and puncture (CLP). Muscle atrophy progressively worsened during the course of sepsis, reached a significant deterioration on the 3rd day after CLP, and then was followed by a subsequent recovery as demonstrated by evaluations of included body weight, muscle weight, and cross-sectional area (CSA) of the tibialis anterior (TA) and gastrocnemius (GA) muscles (Fig. 2a–c and Supplementary Fig. 1a, b, d–g). However, muscle weight and cross-sectional area of the soleus muscle (SO) did not change significantly (Supplementary Fig. 1c, h–j).

We identified increased expression of atrogenes, including the ubiquitin ligases *Fbxo32* (Atrogin-1) and *Trim63* (MuRF1), known as markers of muscle atrophy[21], on 1st and 3rd day after CLP in TA, GA, and SO muscles (Fig. 2d and Supplementary Fig. 1k, l). Notably, the mRNA levels of *Fbxo32* and *Trim63* in TA and GA muscles were approximately 10-fold higher than those in SO muscle. Functional assessments, including the Kondziela's inverted screen test and grid-hanging capacities, revealed weaker strength in the CLP group, particularly on 3rd day (Supplementary Fig. 2a, b). Consistent with these findings, treadmill running tests showed significantly reduced performance on 3rd day after CLP, gradually recovering over time (Supplementary Fig. 2c–e).

To identify the downstream signaling pathways implicated in skeletal muscle atrophy due to sepsis, we performed transcriptomic analysis of muscles at 3rd day after sham and CLP operation, with 3 mice per group. Gene expression analysis revealed that 228 differentially expressed genes (DEGs) downregulated in CLP-3d muscles were related to oxidative phosphorylation (OXPHOS) and mitochondrion in the top 20 of kyoto encyclopedia of genes and genomes (KEGG) and gene ontology (GO) enrichment (Fig. 2e). In addition, GO enrichment maps related to mitochondrial function and mitochondrial matrix indicated a substantial role for mitochondria in sepsis-induced muscle atrophy (Supplementary Fig. 2f). The abundance of transcriptional coding components of the tricarboxylic acid (TCA) cycle and mitochondrial complexes of the electron transport chain were decreased in the muscles of septic mice (Fig. 2f).

Histological analysis further certified that sepsis reduced the oxidative profile of skeletal muscle, as testified by the lighter staining of succinate dehydrogenase in anterior tibial muscle at 3 days post-CLP compared to the sham group. (Fig. 2g and Supplementary Fig. 2g). Transmission electron microscopy (TEM) revealed altered mitochondrial morphology, including swelling, reduced internal cristae, extensive vacuole formation, and higher mitochondrial injury scores in CLP day 3 muscle (Fig. 2h and Supplementary Fig. 2h). Additionally, adenosine ariphosphate (ATP) synthesis was significantly reduced in CLP samples than in controls (Fig. 2i). These findings collectively indicate a pivotal role of mitochondrial dysfunction in septic muscle atrophy.

S100a8/a9 contribute to sepsis-induced skeletal muscle atrophy and mitochondrial dysfunction

We conducted a detailed analysis of RNA-seq data to identify specific molecules associated with sepsis-induced muscle atrophy and mitochondrial dysfunction. The transcriptomic profiling of skeletal muscle on the 3rd day after CLP revealed a substantial upregulation of genes encoding the calcium-binding proteins S100a8 and S100a9 (Fig. 3a). Time series analysis demonstrated that the mRNA expression of *S100a8/a9* peaked on the 3rd day after CLP, sustained until to the 14th day of sepsis (Fig. 3b, c). This finding was confirmed by immunoblotting analysis (Fig. 3d, e). Correlation analysis revealed a negative association between *S100a8* mRNA expression and total weight, as well as TA and GA muscles weight (Fig. 3f, g, Supplementary Fig. 3a). Additionally, the *S100a8* mRNA level was positively correlated with the expression of the atrophy gene *Fbxo32* (Fig. 3h). Consistent results were observed in the correlation analysis of *S100a9* mRNA expression with muscle mass and body weight (Supplementary Fig. 3b–e). Furthermore, the mRNA expression of *S100a8/a9* showed a negative correlation with ATP content, indicating a potential association with mitochondrial energy production (Fig. 3i and Supplementary Fig. 3f).

To assess whether S100a8/a9 directly induced muscle atrophy and affected mitochondrial ultrastructure and ATP production, we intramuscularly injected recombinant mouse S100a8/a9 protein (rmS100a8/a9) into the GA muscle of wild-type mice for 3 consecutive days. The rmS100a8/a9 protein decreased cross-sectional myofiber area (Fig. 3j, k and Supplementary Fig. 3g) and increased the expression of the atrophy gene *Fbxo32* compared to controls (Fig. 3l). Additionally, rmS100a8/a9-treated mice exhibited aggravated mitochondrial damage (Fig. 3m, n) and reduced ATP levels (Fig. 3o), indicating that S100a8/a9 impairs muscle mitochondrial ultrastructure and energy production function and induces muscle atrophy.

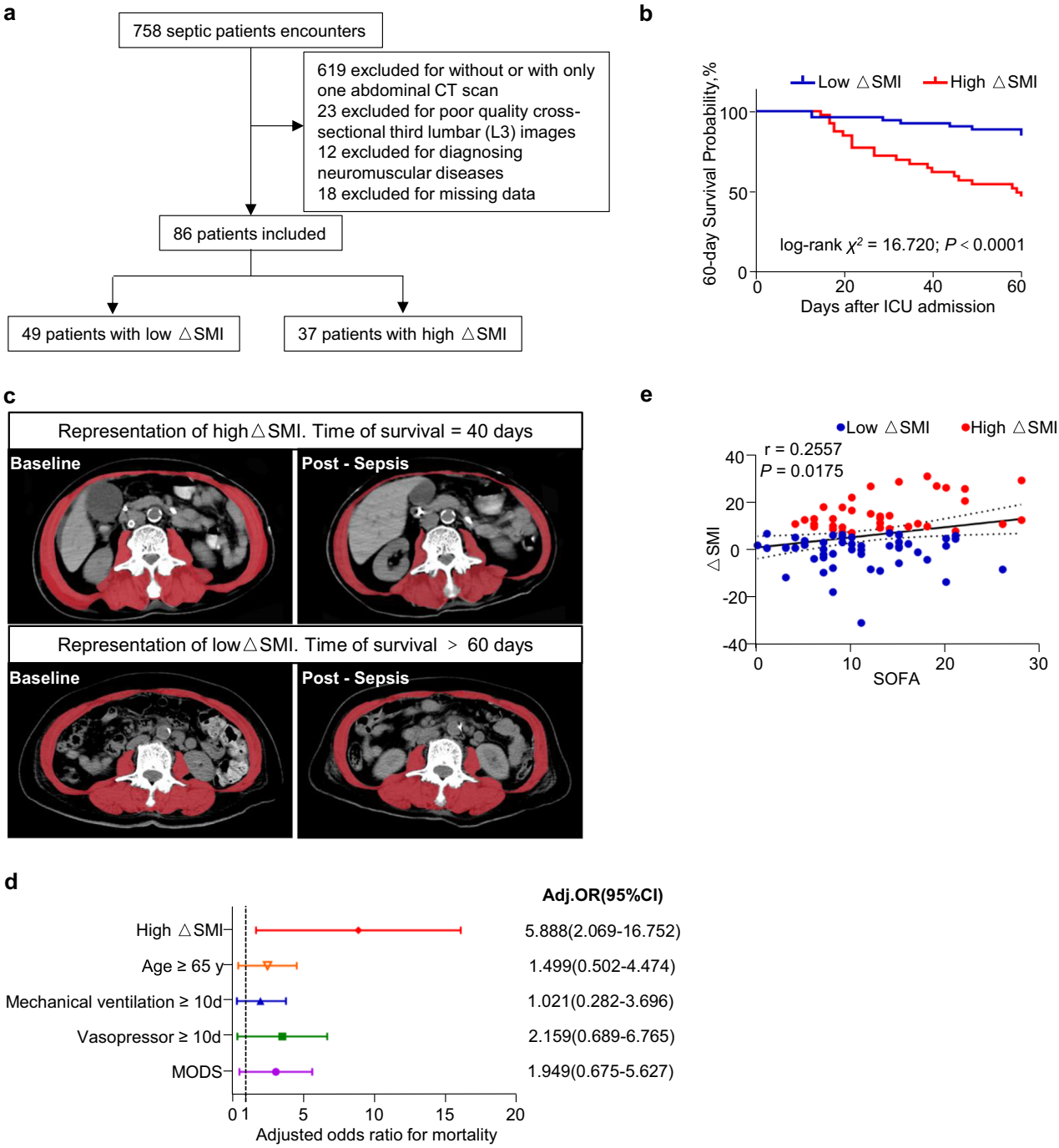

Fig. 1 | The high skeletal muscle index (△SMI) is an independent risk factor for 60-day mortality in septic patients. a Study flow diagram for septic patients. **b** Kaplan–Meier survival curves (60-day) stratified by △SMI. **c** Representative CT scans at the third lumbar vertebra level in two septic patients at baseline and post-sepsis. The red shadows show the skeletal muscle area. **d** Adjusted 60-day mortality according to △SMI category, age, MODS, vasopressor, and mechanical ventilation, is analyzed by multivariable logistic regression. The values shown are the adjusted odds ratio (aOR, 95% confidence interval). Low △SMI, Age <65 y, Mechanical ventilation <10 d, Vasopressor <10 d, non-MODS are defined as reference. **e** Correlation of the △SMI level with sequential organ failure assessment (SOFA) score. Data are presented as Two-tailed Spearman's rank correlation. The adjusted odds ratios with 95% confidence intervals are shown. Each dot represents an individual subject.

To investigate whether blocking S100a8/a9 could rescue mitochondrial ultrastructure and energy production function and alleviate sepsis-induced muscle atrophy, we intraperitoneally injected the S100a8/a9 inhibitor paquinimod or vehicle for 3 consecutive days after CLP. Paquinimod is a selective inhibitor of S100a8/a9, which specifically blocks the function of S100a8/a9 by preventing S100a8/a9 binding to RAGE and TLR4[22,23]. Paquinimod-treated septic mice showed increased diameter single muscle fibers (Fig. 3p and Supplementary Fig. 3h, i) and reduced expression of atrogenes (Fig. 3q and Supplementary Fig. 3j–m). Analysis of mitochondrial shape and function revealed that paquinimod-treated mice exhibited significantly improved mitochondrial morphology (Fig. 3r) and increased ATP synthesis (Fig. 3s). Muscle strength assessments demonstrated that paquinimod treatment maintained certain muscle strength and increased grid-hanging capacities (Fig. 3t and Supplementary Fig. 3n). In terms of athletic

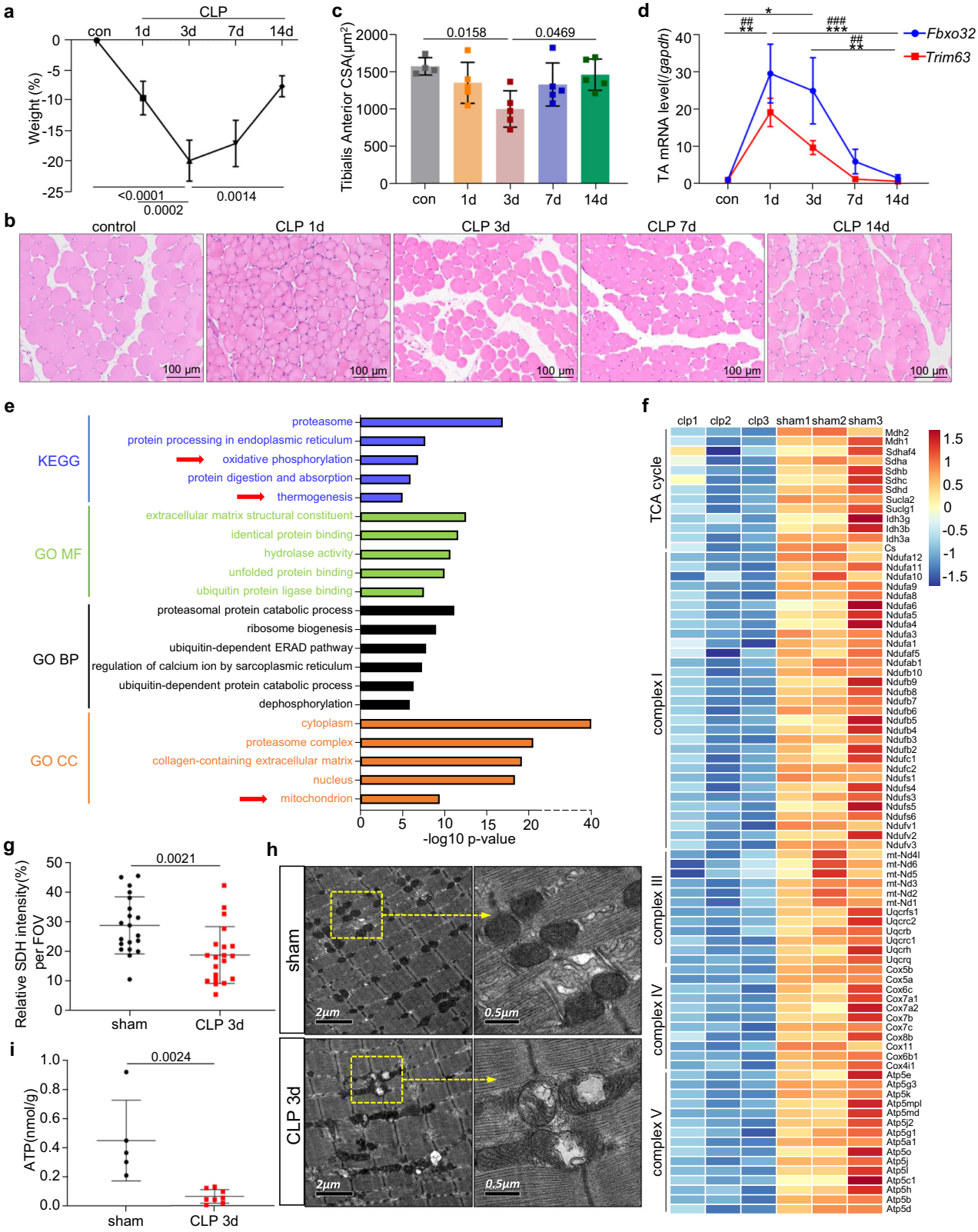

ability, paquinimod-treated septic mice exhibited significant increases in maximal speed, time, and distance to exhaustion (Fig. 3u, v and Supplementary Fig. 3o). These findings suggest that the inhibition of S100a8/a9 can improve mitochondrial ultrastructure and energy production function and mitigate loss of muscle mass and strength in sepsis.

S100a8/a9 induces skeletal muscle atrophy via RAGE

S100a8/a9 is an endogenous ligand of Toll-like receptor 4 (TLR4) and RAGE. So, we treated wide-type, *Rage*$^{-/-}$ and *Tlr4*$^{-/-}$ mice with vehicle or rmS100a8/a9 for 3 days (Fig.4a). RAGE deficiency effectively prevented muscle atrophy during sepsis, including maintaining the cross-sectional

Fig. 2 | Skeletal muscle atrophy is associated with mitochondrial dysfunction in septic mouse model. a Body weight at 0 and 1, 3, 7, and 14 days after CLP. (control and CLP 14 d, $n = 6$ mice; CLP 1 d and 3 d, $n = 15$ mice; CLP 7 d, $n = 12$ mice) **b** Representative haematoxylin and eosin (H&E) staining images from tibialis anterior (TA) at 0, 1, 3, 7, and 14 days after CLP. Scale bars, 100 μm. **c** Fiber CSA (μm^2) of TA muscle from 0 day up to 14 days after CLP. (control, $n = 4$ mice; CLP 1 d, 3 d, 7 d and 14 d, $n = 5$ mice). **d** *Fbxo32* and *Trim63* expression (mRNA) in TA muscle. ($n = 5$ per group). $^{*}p < 0.05$, $^{**}p < 0.01$, $^{***}p < 0.001$ of *Fbxo32* mRNA level, $^{\#\#}p < 0.01$, $^{\#\#\#}p < 0.001$ of *Trim63* mRNA level. **e** Part of the top 20 of KEGG and GO enrichment analysis of muscles from CLP-3d or sham-3d group. ($n = 3$ per group). Red arrows indicate mitochondria related pathways. **f** Heatmap of genes encoding metabolic enzymes involved in the TCA cycle and metabolic enzymes contributing to the electron transport chain 3 d after CLP or sham. ($n = 3$ per group). Gene expression values expressed as $\log_2$(FC). FC: fold change. **g** Quantification of succinate dehydrogenase (SDH) staining intensity of TA cross-section. graph showing SDH staining intensity per field of view (FOV). Each symbol represents a FOV of SDH images. Each group has 5 mice and 4 FOVs were randomly selected for assay from each animal. **h** Representative intermyofibrillar mitochondria transmission electron microscopy (TEM) images of TA muscle 3 d after CLP or sham. **i** Graphs showing the level of total ATP in TA muscles 3 d after CLP or sham. (sham, $n = 5$ mice, CLP 3 d, $n = 8$ mice). Bars show mean ± SEM (**c**, **g**, **i**) and median with interquartile range (**a**, **d**). Two-sided *P* values were determined by one-way analysis of variance (ANOVA), followed by Tukey's multiple comparison test (**c**), the Kruskal–Wallis with Dunn's multiple comparison test (**a**, **d**), and unpaired t-test (**g**, **i**).

myofiber area (Fig.4b–d and Supplementary Fig. 4a–d) and reducing the expression of *Fbxo32* mRNA (Fig.4e). Moreover, we detected a higher *Rage* expression in muscle of rmS100a8/a9-treated mice as well as CLP model (Fig.4f, g). The GO enrichment analysis of RNA sequencing data also indicated that RAGE binding pathway is aggregated in the muscles of CLP mice (Fig.4h). Collectively, these data indicated that S100a8/a9-RAGE is the major signaling pathway involved in sepsis-induced muscle atrophy.

RAGE deficiency improves muscle mitochondrial morphology and ATP generation and alleviates skeletal muscle atrophy in sepsis

The analysis of RNA-seq data revealed that the expression of the majority of genes related to the TCA cycle and mitochondrial complexes was increased in $Rage^{-/-}$ mice compared with wild-type (WT) mice, indicating that the protective effect of RAGE deficiency on mitochondrial function is transcriptionally regulated (Fig. 5a). Specifically, RAGE deficiency enhanced the oxidative phosphorylation subunit expression of the TA muscle, particularly the core subunits of complex I (Fig. 5a). Meanwhile, the septic $Rage^{-/-}$ mice exhibited more intense succinate dehydrogenase activity compared to control mice (Fig. 5b and Supplementary Fig. 5a). Additionally, TEM analysis revealed that $Rage^{-/-}$ mice displayed improved mitochondrial morphology (Fig. 5b–e). These results, coupled with the observed increase in ATP synthesis in $Rage^{-/-}$ septic mice (Fig. 5f), suggest that RAGE deficiency can alleviate muscle mitochondrial dysfunction in sepsis.

The effect of RAGE deficiency in septic skeletal muscle was further investigated. The lower body weight (Fig. 5g) and reduced TA and GA muscle mass happened in WT septic mice (Fig. 5h and Supplementary Fig. 5b), which were mitigated in $Rage^{-/-}$ septic mice. Moreover, $Rage^{-/-}$ septic mice displayed an increased cross-sectional myofiber area (Fig. 5i–k and Supplementary Fig. 5c–e) and reduced expression of *Fbxo32* (Atrogin-1) and *Trim63* (MuRF1) (Fig. 5l and Supplementary Fig. 5f–i). Functional assessments, including grid-hanging capacity, weight tests, and treadmill exhaustion tests, revealed significantly worse results for WT septic mice (Fig. 5m–p and Supplementary Fig. 5j), however, all these impairments were alleviated in $Rage^{-/-}$ septic mice. These findings underscore the RAGE deficiency protects skeletal muscle from atrophy through improving mitochondrial morphology and increasing ATP generation in sepsis.

S100a8/a9-RAGE triggers Drp1 phosphorylation-mediated muscle mitochondrial fragmentation in sepsis

To investigate the mechanism through which S100a8/a9-RAGE affects septic mitochondrial dysfunction and atrophy, we conducted high-resolution confocal imaging of mitochondrial networks in the frozen sections of extensor digitorum longus (EDL) muscles. In WT septic mice, fragmented mitochondrial networks were observed, characterized by disorganization and uneven distributions across the fibers, in contrast to the normal mitochondrial network preserved in $Rage^{-/-}$ septic mice (Fig. 6a).

Considering the abnormalities in the mitochondrial network, we hypothesized an imbalance in mitochondrial dynamics regulated by RAGE in septic amyotrophy. Phosphorylation of Drp1 (Ser616) was elevated in WT septic mice compared with WT sham mice, while there was no significant difference in the levels of mitochondrial proteins Mfn2, Opa1, and Fis1 (Fig. 6b, c and Supplementary Fig. 6a–e). In contrast, $Rage^{-/-}$ mice did not exhibit increased phosphorylation of Drp1 (Ser616) or alterations in other mitochondrial proteins (Fig. 6b, c and Supplementary Fig. 6a–e). These findings suggest that RAGE deficiency prevents mitochondrial fission by reducing phosphorylation of Drp1 (Ser616) in sepsis.

Furthermore, we observed that the inhibition of S100a8/a9 improved mitochondrial length and area (Fig. 6d–f). Additionally, vehicle-treated septic muscles displayed fragmented cristae and vacuolar mitochondria, whereas paquinimod-treated and control mice exhibited compact cristae in normal mitochondria (Fig. 6d). The level of p-Drp1^{ser616} protein was increased in vehicle-treated septic mice compared to paquinimod-treated septic mice (Fig. 6g, h and Supplementary Fig. 6f). These results indicate that the S100a8/a9-RAGE signaling pathway activates phosphorylated Drp1^{ser616}, promoting mitochondrial fission and damage that ultimately lead to septic muscle atrophy.

Inhibition of Drp1 ameliorates septic muscle atrophy by improving mitochondrial morphology and ATP generation

Finally, we investigated whether inhibiting mitochondrial fission could protect mitochondrial ultrastructure and energy production function and alleviate muscle atrophy after sepsis (Fig. 7a). Briefly, the Drp-1 inhibitor, Mdivi-1 (10 mg/kg), or PBS was administered intraperitoneally for 3 consecutive days after CLP surgery, with sham-operated mice used as controls. TEM revealed that muscles treated with Mdivi-1 had a lower mitochondrial injury score, longer mitochondria (Fig. 7b–d), and increased ATP synthesis (Fig. 7e) in septic mice. This suggests that Mdivi-1 promotes the recovery of mitochondrial ultrastructure and improves muscle ATP generation during sepsis.

We then performed cross-sectional area (CSA) analysis and found that Mdivi-1-treated septic mice presented larger myofibers and a rightward shift in myofiber size (Fig. 7f–h). Mdivi-1 treatment also attenuated the expression of atrogenes in septic muscle, such as Atrogin-1 (*Fbxo32*) and MuRF1 (*Trim63*), as demonstrated by quantitative real-time polymerase chain reaction (qRT-PCR) (Fig. 7i, j) and western blot analysis (Fig. 7k–m). Furthermore, compared with vehicle-treated septic mice, Mdivi-1 treatment in septic mice improved lattice suspension capacity (Fig. 7n), weight test performance (Fig. 7o), maximum speed (Fig. 7p), running time (Fig. 7q) and distance to exhaustion (Fig. 7r). These results suggest that Mdivi-1 ameliorates sepsis-induced muscle atrophy by inhibiting mitochondrial fission and improving mitochondrial ultrastructure and energy production function.

Discussion

Skeletal muscle atrophy poses a significant challenge in septic patients, with a high change in skeletal muscle index (△SMI) emerging as an independent risk factor for 60-day mortality. Our investigation further revealed that S100a8/a9-RAGE signaling triggered mitochondrial fission through Drp1 phosphorylation, leading to septic skeletal muscle atrophy. Encouragingly, intraperitoneal injection of the Drp1 inhibitor Mdivi-1 demonstrated the potential to prevent muscle atrophy, suggesting

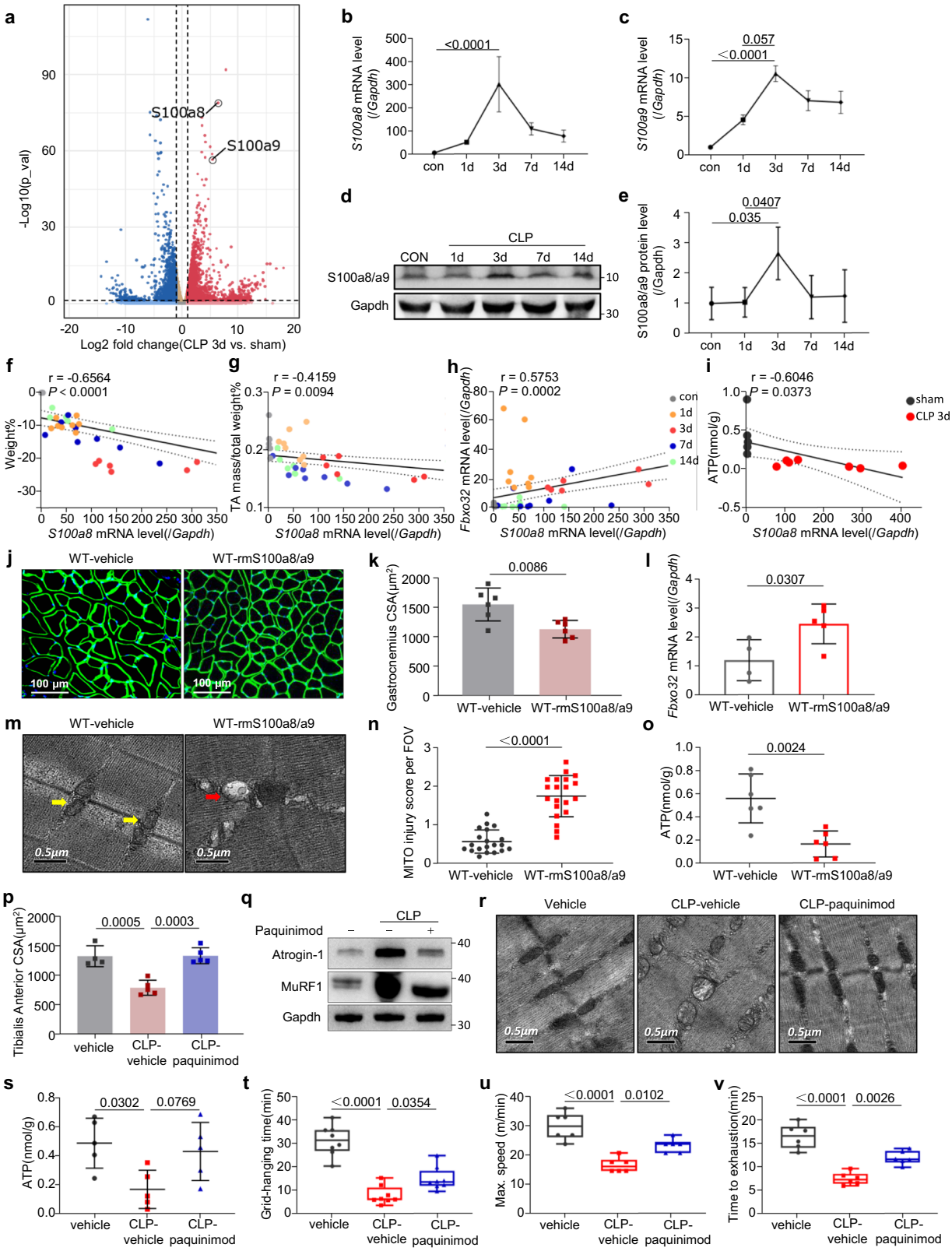

that targeting S100a8/a9-RAGE-initiated mitochondrial fission may offer a therapeutic avenue against septic muscle atrophy.

Skeletal muscle atrophy affects 40–70% of septic patients, predominantly contributing to Intensive Care Unit-Acquired Weakness (ICUAW)[2]. In our retrospective clinical cohort study, a substantial 55.81% of septic patients were identified as sarcopenic at hospital discharge, and faced complications related to muscle atrophy. The high △SMI cohort exhibited significant loss of skeletal muscle as the sepsis progressed, with a significantly increased 60-day mortality. Notably, baseline sarcopenia, as opposed to acute muscle wasting, emerged as the primary predictor of mortality in critically ill patients[24]. Divergent enrollment criteria, patient age, and small sample sizes may account for varying results in previous studies.

Fig. 3 | S100a8/a9 contribute to sepsis-induced skeletal muscle atrophy and mitochondrial dysfunction. a Volcano plots showing the gene expression fold change (x-axis, log2 scale) and p-value significance (y-axis, -log10 scale) of CLP 3 d versus sham 3 d skeletal muscles. Dotted lines indicate a Log_{10}FDR threshold of >0.05 or Log_2FC (fold change) of ±2. ($n = 3$ per group). Expression level of *S100a8*(**b**) and *S100a9*(**c**) measured by qPCR in tibialis anterior (TA) muscle at 0 and 1, 3, 7, and 14 days after CLP ($n = 7$ per group). Representative western blots images (**d**) and quantification protein levels of S100a8/a9 (**e**) in TA muscle at 0 and 1, 3, 7 and 14 days after CLP ($n = 4$ per group). Correlation of *S100a8* mRNA expression with total weight (**f**), TA muscle weight (**g**), and *Fbxo32* mRNA expression (**h**). Each symbol represents one animal (control, $n = 8$ mice; CLP 1 d, $n = 8$ mice; CLP 3 d, $n = 7$ mice; CLP 7 d, $n = 8$ mice; CLP 14 d, $n = 7$ mice). **i** Correlation of *S100a8* mRNA expression with ATP content. Each symbol represents one animal (sham 3 d, $n = 5$ mice; CLP 3 d, $n = 7$ mice). Data are presented as Two-tailed Spearman's rank correlation. Dots represent individual subjects. Dashed lines represent 95% confidence intervals. **j** Representative gastrocnemius (GA) cross-section 3-days after intramuscular injection with rmS100a8/a9 or vehicle reagent. DAPI, blue; laminin, green. Scale bar, 100 μm. **k** Fiber CSA (μm²) of GA muscle in (**j**). ($n = 6$ per group). **l** mRNA expression level of *Fbxo32* 3-days after intramuscular injection with rmS100a8/a9 or vehicle reagent ($n = 4$–5 per group). **m** Representative images of GA intermyofibrillar mitochondria by TEM after intramuscular injection with rmS100a8/a9 or vehicle reagent. Scale bars, 0.5 μm. **n** Mitochondria injury score from the statistics of (**m**). Bar graph presents mitochondrial injury score per FOV. Each symbol represents a TEM image of one FOV. There were 4 mice per group, and 5 FOVs were randomly selected for statistic from each animal. **o** Total ATP content in GA muscles after intramuscular injection with rmS100a8/a9 normalized to vehicle. ($n = 6$ per group). **p** Graph showing fiber CSA (μm²) of TA muscle after intraperitoneally injection with paquinimod or vehicle reagent for 3 consecutive days after CLP. (vehicle, $n = 4$ mice; CLP- vehicle, $n = 5$ mice; CLP- paquinimod, $n = 5$ mice). **q** The representative western blots images of Atrogin-1 and MuRF1 in muscle tissue lysates after intraperitoneally injection with paquinimod or vehicle reagent for 3 consecutive days after CLP. **r** Representative TEM images of TA intermyofibrillar mitochondria. Scale bars, 0.5 μm. **s** Graph showing the levels of total ATP in the muscle tissue lysates ($n = 5$ per group). Graphs showing grid-hanging capacity (**t**), treadmill maximal speed (**u**), run time to exhaustion (**v**). (**t**, $n = 8$ mice per group; **u**, **v**, $n = 6$ mice per group). Bars show mean ± SEM (**e**, **k**, **l**, **o**, **p**, **s**–**v**) and median with interquartile range (**b**, **c**, **n**). Two-sided *P* values were determined by unpaired t-test (**k**, **l**, **o**) and Mann–Whitney U-test (**n**), and one-way ANOVA, followed by Tukey's multiple comparison test (**e**, **p**, **s**–**v**), the Kruskal–Wallis with Dunn's multiple comparison test (**b**, **c**).

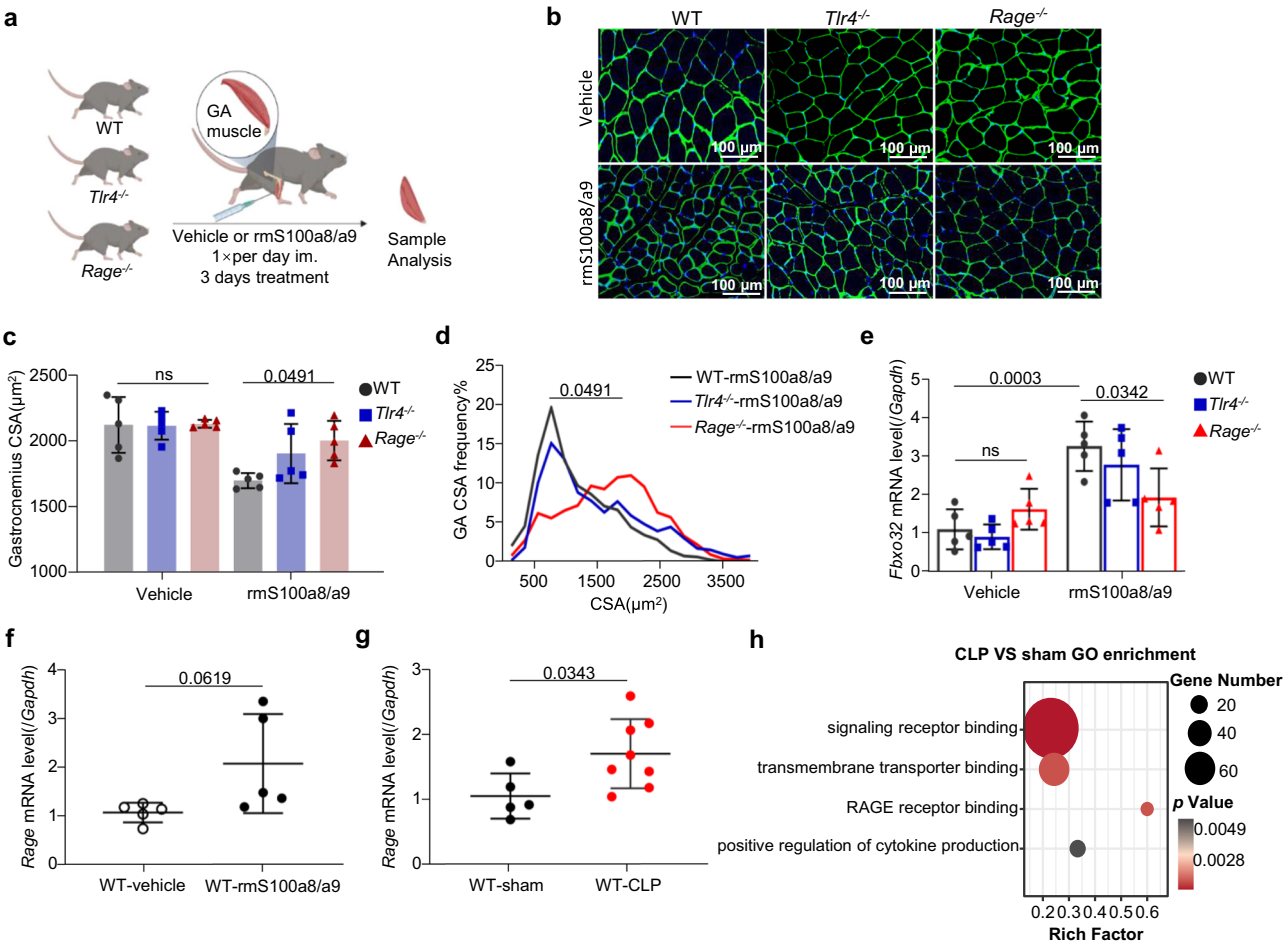

Fig. 4 | S100a8/a9 induces skeletal muscle atrophy via RAGE. a Experimental scheme showing gastrocnemius muscles of WT, *Rage*$^{-/-}$ and *Tlr4*$^{-/-}$ mice injected with rmS100a8/a9 (100 ng/muscle) or vehicle (PBS) for three consecutive days. Representative gastrocnemius (GA) cross-section images (**b**) and quantitative analysis of fiber CSA (μm²) (**c**) and distribution of CSA area (**d**, %) after rmS100a8/a9 treatment ($n = 5$ per group). DAPI, blue; laminin, green. Scale bar, 100 μm. **e** Graph showing mRNA level of *Fbxo32* in the GA muscle by qPCR ($n = 5$ per group). **f** Graph showing mRNA level of *Rage* 3 days after intramuscular injection with rmS100a8/a9 or vehicle reagent in the GA muscle by qPCR ($n = 5$ per group). **g** Graph showing mRNA level of *Rage* 3 days after CLP or sham operation in the TA muscle by qPCR (sham, $n = 5$ mice; CLP, $n = 8$ mice). **h** GO analysis of RAGE receptor-related pathways between CLP 3 d and sham controls ($n = 3$ per group). Bars show mean ± SEM (**c**, **e**, **f**, **g**). ns, not significant. Two-sided *P* values were determined by unpaired t-test (**f**, **g**), one-way ANOVA with Games-Howell's multiple comparisons test (**c**), and two-way ANOVA with Tukey's multiple comparisons test (**e**).

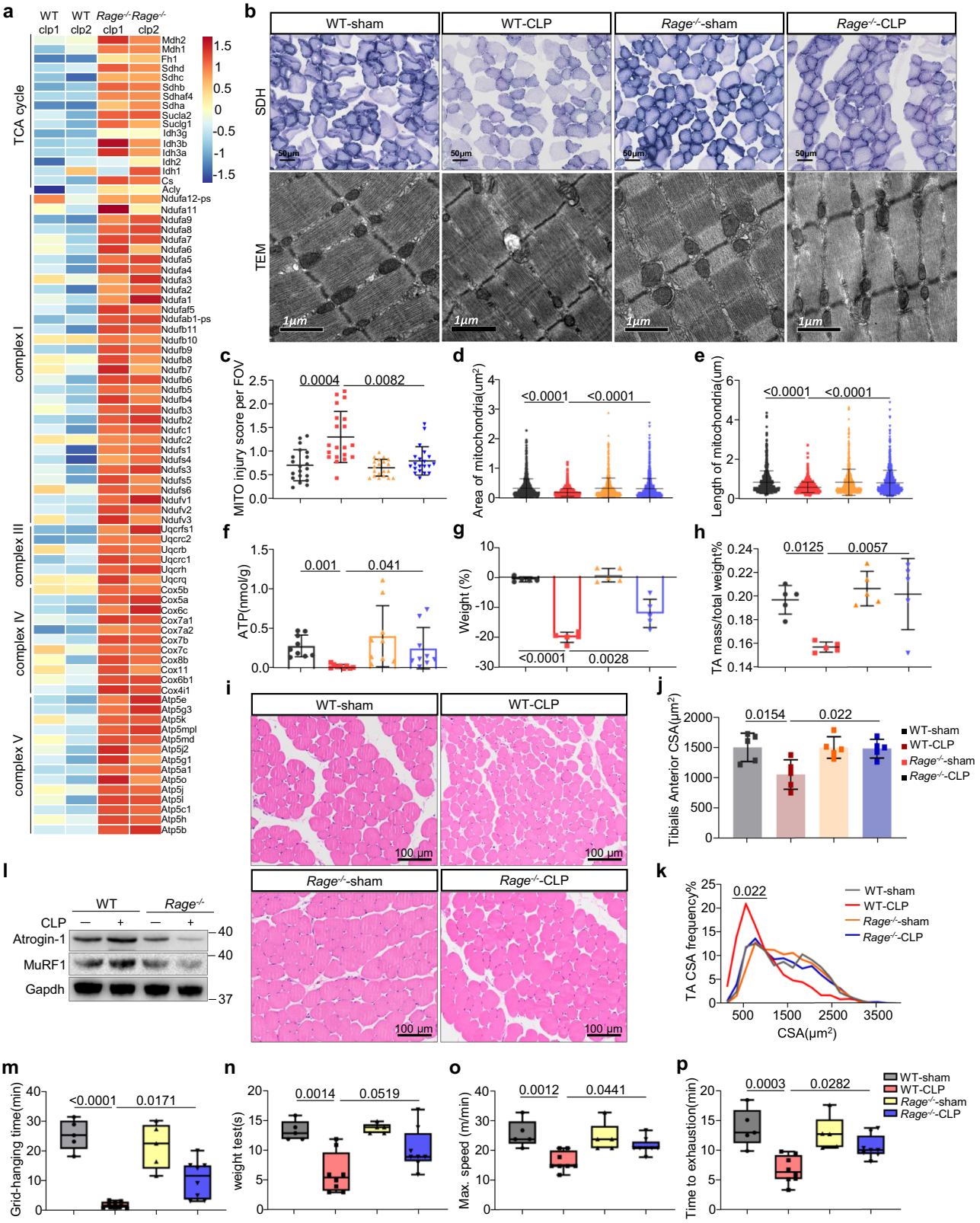

Importantly, even after excluding diabetic patients, the high △SMI group still exhibited significantly higher 60-day mortality than the low △SMI group. Furthermore, in this study, with the association of SOFA score, high △SMI is considered to be correlated with increased disease severity and heightened 60-day mortality.

Skeletal muscle atrophy is a multifactorial disease associated with dysregulation of signaling pathways related to persistent intrinsic tissue inflammation, defective mitochondria, injuring sarcolemmal membranes, and disrupted proteostasis in sepsis[16,17]. In particular, mitochondria dysfunction plays a crucial role in the pathology of skeletal muscle atrophy and

Fig. 5 | RAGE deficiency improves muscle mitochondrial morphology and ATP generation and alleviates skeletal muscle atrophy in sepsis. a Heatmap of genes encoding metabolic enzymes involved in the TCA cycle and metabolic enzymes contributing to the electron transport chain. Gene expression values were expressed as log2(FC) comparing *Rage*$^{-/-}$ and WT mice 3-days after CLP model. (n = 3 per group) FC: fold change. **b** Representative images of succinate dehydrogenase (SDH) staining (above, Scale bar, 50 μm.) and TEM (below, Scale bar, 1 μm.) of WT and *Rage*$^{-/-}$ mice 3 d after CLP or sham operations in tibialis anterior (TA) muscle tissue. **c** Graph showing mitochondria injury score of *Rage*$^{-/-}$ and WT 3 days after CLP or sham operation in TA muscle tissue. Bar graph presents mitochondrial injury score per FOV. Each symbol represents a TEM image of one FOV. There were 4 mice per group, and 5 FOVs were randomly selected for statistic from each animal. **d**, **e** Quantitative analysis of Intermyofibrillar (IMF) mitochondria area and length from TEM images as in (**b**) (n = 4 per group, total mitochondria quantified: n = 801 wt sham, n = 834 wt CLP, n = 769 *Rage*$^{-/-}$ sham, n = 863 *Rage*$^{-/-}$ CLP). **f** Graph showing the levels of total ATP in TA muscle tissue lysates of WT and *Rage*$^{-/-}$ mice 3 d after CLP or sham operations (n = 9 per group). Graphs showing the body weight (**g**) and TA muscle weight (**h**) of *Rage*$^{-/-}$ and WT 3-days after CLP or sham operations (n = 5 per group). Representative TA cross-section H&E images (**i**) and quantitative analysis of fiber CSA (μm^2) (**j**) and distribution of CSA area (**k**, %) of WT and *Rage*$^{-/-}$ mice 3 d after CLP or sham operations (n = 5 per group). Scale bar, 100 μm. **l** Graph showing the representative western blots images of Atrogin-1 and MuRF1 in muscle tissue lysates. Graphs showing grid-hanging capacity (**m**), weight test(**n**), treadmill maximal speed (**o**), run time to exhaustion (**p**) of WT and *Rage*$^{-/-}$ mice 3 d after CLP or sham operations. (sham, n = 5 mice, CLP, n = 8 mice). Bars show mean ± SEM (**g**, **h**, **j**, **m**–**p**) and median with interquartile range (**c**–**f**). Two-sided P values were determined by two-way ANOVA with Tukey's multiple comparisons test (**g**, **h**, **j**, **k**, **m**–**p**) and with Sidak's multiple comparisons test (**c**–**f**).

weakness[6,7]. Our transcriptome analysis revealed that the abundance of mitochondrial respiratory complexes genes was substantially downregulated in the skeletal muscle during sepsis. We confirmed that S100a8/a9-RAGE signaling impairs mitochondrial function and aggravates muscle atrophy. Additionally, among the top 20 KEGG and GO pathways, those related to the endoplasmic reticulum (ER) and calcium ion regulation were also activated, which are closely associated with muscle atrophy. The ER is a highly specialized organelle that assures calcium homeostasis and therefore muscle contraction in muscle cells. Previous studies have shown that ER stress promotes sepsis-induced muscle atrophy via activation of STAT3[25]. Moreover, Mitochondria and ER have a synergistic relationship and serve as critical regulatory hubs for regulation skeletal muscle metabolism[26]. However, the exact cooperative mechanism between the ER and mitochondria in the pathogenesis of sepsis-induced muscle atrophy remains elusive, meriting further investigation. Our study focused on the mitochondrial dysfunction and was evident that mitochondrial dysfunction is considered as a major factor in sepsis-induced muscle atrophy, highlighting the need to identify a biomarker that signals the initiation of muscle mitochondrial dysfunction in sepsis. Inflammatory mediators act as triggers for sepsis-induced muscle atrophy[16,17], directly impacting mitochondrial respiration and energy supply in various models[16,27].

S100a8 and S100a9, members of the calcium-binding S100 protein family, form a heterodimer and are recognized as highly sensitive biomarkers in inflammatory processes[28]. Previous studies have reported that S100a8/a9 complexes directly mediate myocardial apoptosis, autophagy, and mitochondrial function in sepsis-associated cardiac complications[29–31]. Transcriptomic analysis in previous study revealed a significant upregulation of the inflammatory molecules S100a8/a9, with increased expression persisting throughout the sepsis process, even up to 28 days after sepsis[32]. Notably, in the current study, this upregulation was associated with muscle atrophy and reduced ATP synthesis.

Furthermore, our study demonstrated that local intramuscular injection of recombinant S100a8/a9 protein promoted muscle atrophy, while pharmacological blockade of S100a8/a9 protected mice from septic myopathy. The S100a8/a9 inhibitor, paquinimod, has been extensively studied in sepsis models. Paquinimod is reported as a potent inhibitor to improve septic cardiomyopathy and liver injury, both of which are associated with enhanced mitochondrial function[33,34]. Paquinimod also has a protective effect on renal dysfunction in sepsis[35]. Here, we expanded the function of paquinimod into rescuing muscle wasting in sepsis. Paquinimod is likely a promising drug for restoring mitochondrial energy supply to prevent muscle atrophy in sepsis. These findings underscore the crucial role of S100a8/a9 in mitochondrial dysfunction, emphasizing its potential as a key target in mitigating sepsis-induced muscle atrophy.

S100a8/a9 complexes are known to bind to both TLR4 and RAGE. However, our investigation revealed that RAGE, rather than TLR4, plays an essential role in mediating S100a8/a9-induced muscle atrophy. In mice lacking the RAGE gene (*Rage*$^{-/-}$), the expression of atrophy genes in the muscle was significantly prevented following intramuscular injection of recombinant mouse S100a8/a9 protein (rmS100a8/a9), whereas this preventive effect was not observed in mice lacking the TLR4 gene (*Tlr4*$^{-/-}$). It is worth noting that high Ca^{2+} concentrations can impede the interaction between S100a8/a9 and TLR4[36]. This preference for RAGE over TLR4 in mediating S100a8/a9-induced muscle atrophy may be associated with the disruption of Ca^{2+} homeostasis in the muscle during sepsis[37]. Although we did not directly monitor Ca^{2+} concentration, our RNA-seq analyses indicate that the RAGE binding pathway is activated.

Furthermore, our study revealed an enhanced production of S100a8/a9 in response to RAGE activation, contributing to the conceptualization of a vicious circle of RAGE mediation during inflammation[38]. Knockout of RAGE resulted in a downregulated expression of S100a8/a9 in septic mice, emphasizing the pivotal role of RAGE in sustaining the S100a8/a9-induced septic muscle atrophy.

RAGE signaling is integral to skeletal muscle physiology[39], and its aberrant activity is a hallmark of muscle atrophy occurring in response to various conditions such as cancer, diabetes, aging, and genetic disorders[39–41]. Previous studies have elucidated that RAGE activation can directly influence mitochondrial function by impacting NADPH oxidase and the mitochondrial electron transport chain, leading to the overproduction of reactive oxygen species (ROS)[38]. Furthermore, the activation of the RAGE-ligand axis diminishes cellular stress defenses in the muscles of metabolic diseases[42]. It has been suggested that RAGE activation promotes mitochondrial fission in different disease models[43,44].

Mitochondrial fission is orchestrated by membrane-associated adaptors and executed by the dynamin-like GTPase Drp1, which is recruited to the outer mitochondrial membrane and forms helical oligomers inducing membrane constriction and severing[45]. In addition, the extracellular signal-regulated kinase (Erk) pathway is involved in the increased phosphorylation of the mitochondrial protein Drp1 at serine 616 following RAGE activation[44]. Our results underscore that the S100a8/a9-RAGE axis induces Drp1 phosphorylation, leading to muscle mitochondrial fragmentation. Future studies could delve into the specific role of Erk in this process.

A central discovery of this study is that inflammation disturbance in sepsis induces mitochondria fission in skeletal muscle, that is regulated by Drp1 phosphorylation. Our findings underscore the critical role of mitochondria fission in skeletal muscle during sepsis, which is pivotal in determining muscle atrophy and weakness. Skeletal muscles, containing highly structured and metabolically active cells, rely on a well-functioning network of mitochondria to sustain optimal ATP supply, which is essential for healthy muscle contractions and mass[46]. Disruption of the mitochondrial network leads to a disturbance in cellular energy metabolism[13]. Our investigation revealed a reduction in intracellular ATP levels in skeletal muscle during sepsis that attribute to increased mitochondrial fragmentation. Previous research has demonstrated that overexpression of Drp1 triggers organelle dysfunction and activates AMPK, initiating the FoxO3-mediated atrophy program[47,48]. Our study shows that muscle Drp1 activity is increased and regulated by phosphorylation during sepsis without affecting total Drp1 protein or Drp1 mRNA expression. However, the regulatory mechanism by

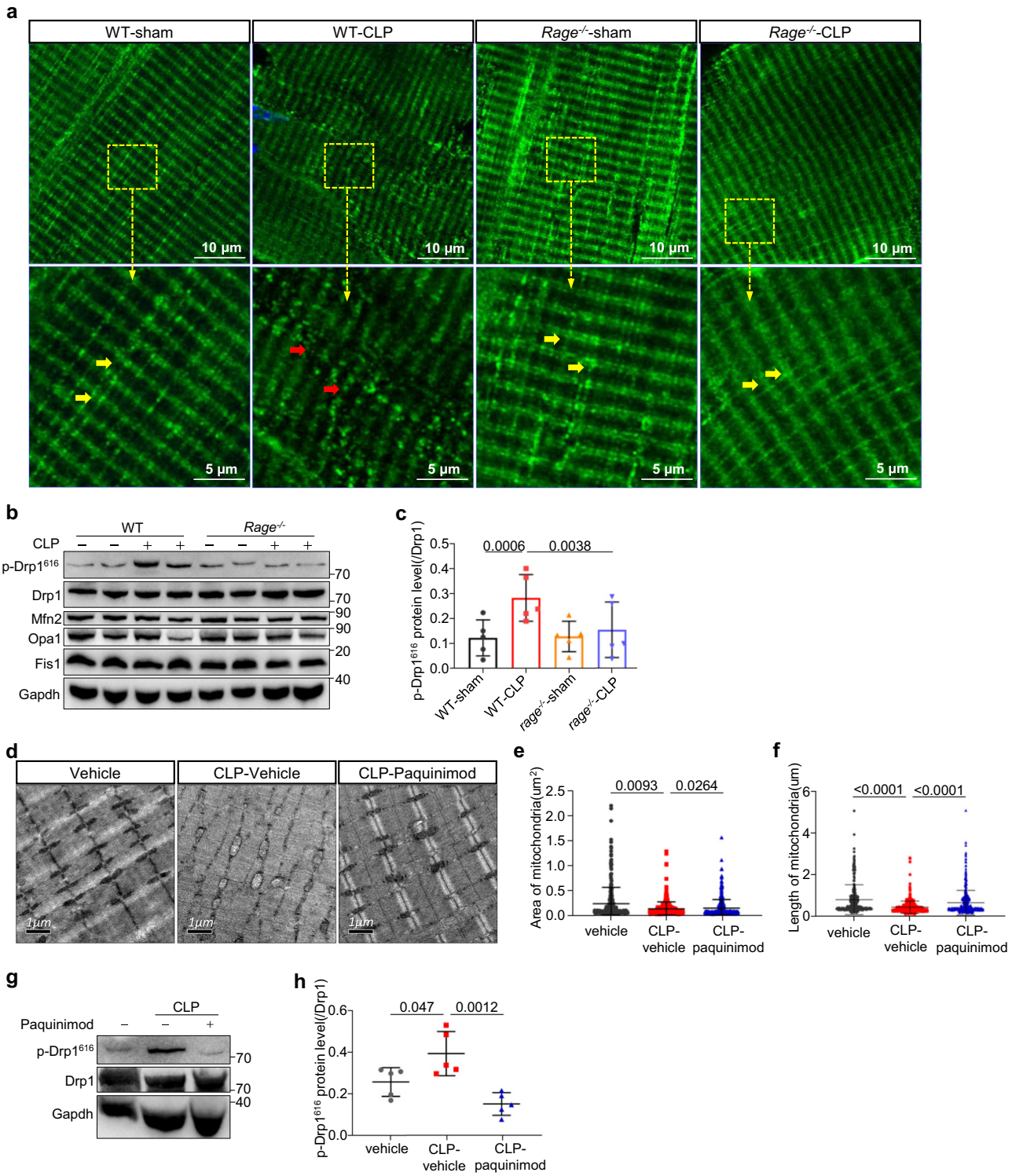

Fig. 6 | S100a8/a9-RAGE triggers Drp1 phosphorylation-mediated muscle mitochondrial fragmentation in sepsis. a Representative confocal images of the mitochondrial network (VDAC, green) in EDL muscle fibers of WT and *Rage*$^{-/-}$ mice 3 d after CLP or sham operations. Yellow arrows show the longitudinal pattern of interconnected mitochondria alongside the myofibrils, and the red arrows show the mitochondrial disconnection. VDAC: voltage-dependent anion channel. Scale bar, 10 μm and 5 μm. **b** Representative images of western blots of mitochondrial dynamics regulatory proteins (p-Drp1^{616}, Drp1, Fis1, Mfn2, and Opa1) of WT and *Rage*$^{-/-}$ mice 3 d after CLP or sham operations in tibialis anterior (TA) muscle tissue lysates. **c** Graph showing the relative protein level of p-Drp1^{616} normalized to Drp1 as reference in (**b**) (n = 5 per group). Representative TEM images (**d**, Scale bar, 1 μm) and quantitative analysis of intermyofibrillar mitochondria area (**e**) and length (**f**) of TA muscle after intraperitoneally injection with paquinimod or vehicle reagent for 3 consecutive days after CLP (n = 4 per group, total mitochondria quantified: n = 291 vehicle, n = 433 CLP vehicle, n = 430 CLP paquinimod). Representative images of western blots of p-Drp1^{616} and Drp1 in TA muscle tissue lysates (**g**) and quantitative analysis of p-Drp1^{616} protein (**h**) 3 days after paquinimod or vehicle treatment with WT septic mice (n = 5 per group). Bars show mean ± SEM (**c**, **h**) and median with interquartile range (**e**, **f**). Two-sided P values were determined by two-way ANOVA with Tukey's multiple comparisons test (**c**), one-way ANOVA with Tukey's multiple comparison test (**h**), and the Kruskal–Wallis with Dunn's multiple comparison test (**e**, **f**).

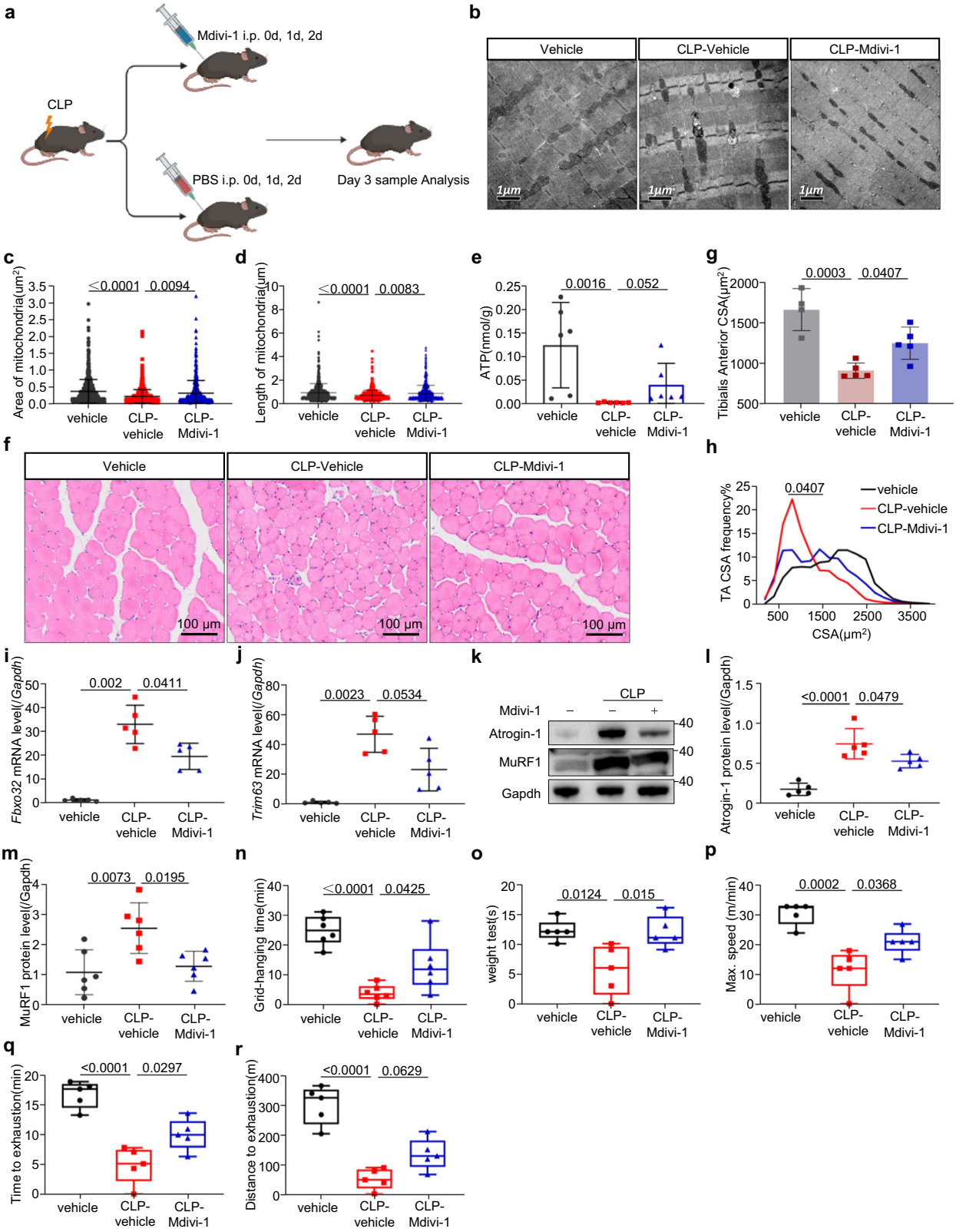

which Drp1 initiates the muscle atrophy program during sepsis remains undefined and requires further experimental exploration.

Our data establish the Drp1 inhibitor, Mdivi-1, as a promising therapeutic strategy to mitigate mitochondrial fission-induced muscle atrophy in sepsis. Previous studies have demonstrated the efficacy of Mdivi-1 compounds in attenuating muscle atrophy development by regulating the balance of mitochondrial dynamics in cancer cachexia[49]. Mdivi-1 has also been shown to significantly increase oxidative capacity and muscle contractility in C2C12 cells[50], improve muscle insulin signaling, and enhance systemic insulin sensitivity in obese mice[51]. Additionally, Mdivi-1 treatment has the potential to interrupt the vicious cycle of inflammation via inhibiting the inflammatory cascade and further protecting mitochondrial function[52].

Fig. 7 | Inhibition of Drp1 ameliorates septic muscle atrophy by improving mitochondrial morphology and ATP generation. a Experimental scheme showing WT mice intraperitoneally injected with Mdivi-1(10 mg/kg) or vehicle (PBS) for 3 consecutive days after CLP. Representative TEM images (**b**) and quantitative analysis of intermyofibrillar mitochondria area (**c**) and length (**d**) 3 days after Mdivi-1 or vehicle reagent treated with WT septic mice. Scale bars, 1 μm. ($n = 4$ per group, total mitochondria quantified: $n = 713$ vehicle, $n = 650$ CLP vehicle, $n = 425$ CLP Mdivi-1). **e** Graph showing the level of total ATP in the muscle tissue lysates after intraperitoneally injection with Mdivi-1 or vehicle reagent for 3 consecutive days after CLP ($n = 6$ per group). Representative tibialis anterior (TA) cross-section H&E images (**f**) and quantitative analysis of fiber CSA (μm^2) (**g**) and distribution of CSA area (**h**, %) ($n = 4$-5 per group). Scale bar, 100 μm. Graphs showing the mRNA levels of *Fbxo32* (**i**) and *Trim63* (**j**) in the TA muscle tissue lysates. Western blots images (**k**) and quantitative analysis of Atrogin-1 (**l**) and MuRF1 (**m**) protein levels in muscle tissue lysates 3 days after Mdivi-1 or vehicle treatment with WT septic mice ($n = 5$–6 per group). Graphs showing grid-hanging capacity (**n**), weight test (**o**), treadmill maximal speed (**p**), run time (**q**) and distance(**r**) to exhaustion 3 days after Mdivi-1 or vehicle treatment with WT septic mice ($n = 5$–6 per group). Bars show mean ± SEM (**g**, **i**, **j**, **l**–**r**) and median with interquartile range (**c**–**e**). Two-sided *P* values were determined by one-way ANOVA followed by Tukey's (**g**, **h**, **I**–**o**, **r**) multiple comparisons test, Sidak's multiple comparisons test (**p**, **q**), Games-Howell's multiple comparisons test (**i**, **j**), and Kruskal–Wallis with Dunn's multiple comparison test (**c**–**e**).

In our study, we provide evidence that Mdivi-1 protects mitochondrial function in sepsis while future efforts are needed to unravel the exact mechanism.

In summary, this study identifies S100a8/a9 as a key mediator causing muscle atrophy and provides a mechanistic link between S100a8/a9 and mitochondrial dynamics in septic muscle atrophy. Targeting the S100a8/a9-RAGE signaling-induced Drp1 phosphorylation pathway could be a potential therapeutic strategy for muscle atrophy in sepsis.

Materials and methods

Patients

We conducted a retrospective cohort study involving patients meeting the Sepsis 3.0 clinical criteria at the Intensive Care Unit (ICU) of the First Affiliated Hospital, Zhejiang University School of Medicine, from Jan 2020 to Oct 2022[1]. All enrolled patients underwent two abdominal computed tomography (CT) scans for muscle mass assessment: (i) a baseline diagnostic abdominal CT scan capturing the L3 level within 3 months before sepsis diagnosis; (ii) a post-sepsis abdominal CT scan capturing the L3 level, performed in the ICU after a miniAmum of 5 days of admission following sepsis and before discharge. Exclusion criteria included: (i) age younger than 18 years or older than 90 years; (ii) lack of baseline abdominal CT imaging or inadequate CT images; (iii) poor quality CT images; (iv) concurrent diagnosis of neuromuscular diseases; (v) chemotherapy or radiotherapy within 30 days; (vi) missing data. The study protocol received approval from the Clinical Research Ethics Committee of the First Affiliated Hospital, Zhejiang University School of Medicine (IIT2021369). All ethical regulations relevant to human research participants were followed.

CT protocol

For CT protocol, cross-sectional CT images at the L3 region were typically used to assess the area of skeletal muscle[53]. CT image analysis utilized a Hounsfield unit threshold ranging from −29 to 150 to identify cross-sectional skeletal muscle area at the level of the third lumbar vertebra using Image J software. The cross-sectional area (CSA) of the L3 segment included muscles such as erector spinae, quadratus lumborum, the psoas, internal and external oblique, transverse abdominal, and rectus abdominis. Skeletal muscle index (SMI), widely employed for defining sarcopenia, was calculated by standardizing the CSA of skeletal muscles to the square of height (m) and reported in cm^2/m^2. To quantify longitudinal changes in SMI, we computed the difference (Δ) between baseline and post-sepsis CT and normalized it over a period of 30 days using the formula $\triangle SMI = [($ Baseline SMI (cm^2/m^2) − Post-sepsis SMI (cm^2/m^2)) / (Time between baseline and post-sepsis SMI)$]$ × 30 days. Positive values indicated muscle loss in the time interval. The optimal cutoff value for the continuous variable ΔSMI was determined using receiver operating characteristic (ROC) curve statistics, maximizing the survival difference between the two groups.

Mice and treatments

All animal experiments were reviewed and approved by the Animal Advisory Committee at Zhejiang University and performed according to institutional guidelines (reference no. 20221279). We have complied with all relevant ethical regulations for animal use. C57BL/6 wild-type (WT) mice were purchased from Shanghai SLAC Laboratory Animal Center. C57BL/6J-*Rage*$^{-/-}$ mice were constructed by Nanjing biomedical research institute of Nanjing university via CRISPR/Cas9 technology (Project number XM709828), and have been utilized and reported in other publications[54]. C57BL/10-*Tlr4*$^{-/-}$ mice were purchased from Gempharmatech Co., Ltd. The C57BL/10-Tlr4$^{-/-}$ mice has been widely used and published[55–58]. All mice were bred and maintained under specific pathogen-free conditions in the animal center of Zhejiang University (Hangzhou, China). CLP surgery was performed to induce polymicrobial sepsis in 8–10 week-old male C57BL/6 mice according to a published protocol[59] and prior reported on sepsis-induced muscle atrophy[60,61]. Sham mice were treated identically except for CLP.

For S100a8/a9 overexpression, mice were treated with recombinant mouse S100a8/a9 heterodimer protein (rmS100a8/a9, 100 ng/muscle, R&D Systems, Minneapolis, 8916-S8-050) or phosphate-buffered saline (PBS) as a control in a volume of 20 μl injected intramuscularly for 3 consecutive days.

For S100a8/a9 inhibition, mice were intraperitoneally injected the S100a8/a9 inhibitor paquinimod (10 mg/kg, Sigma-Aldrich, SML2883) or PBS as a control in a volume of 200 μl for 3 consecutive days after CLP.

For Drp1 inhibition, mice were intraperitoneally injected Mdivi-1 (10 mg/kg, MedChemExpress, HY-15886) or PBS as a control in a volume of 200 μl for 3 consecutive days after CLP.

RNA sequencing and differential expression analysis

For RNA-seq analysis, we performed 2 independent studies: one comparing WT mice subjected to sham surgery versus CLP surgery at 3 days post-operation, and the other comparing WT mice with *Rage*$^{-/-}$ mice 3 days post-CLP. Total RNA was extracted from a combination of anterior tibialis and gastrocnemius muscles using Trizol reagent (Thermo Fisher Scientific, 15596018) following the manufacturer's protocol. The quantity and purity of RNA were assessed using the Bioanalyzer 2100 and RNA 6000 Nano LabChip Kit (Agilent, CA, USA, 5067-1511). The average insert size for the final cDNA library was 300 ± 50 bp. cDNA evaluation and sequencing were carried out using the Illumina Novaseq™ 6000 platform (LC Bio Technology CO., Ltd., Hangzhou, China). Genes' differential expression analysis was conducted using the DESeq2 R package between two distinct groups, each consisting of three biological replicates. Genes with a false discovery rate (FDR) below 0.05 and an absolute fold change ≥2 were considered DEGs. Visualization of marker genes, DEGs analysis, Pathway Enrichment Analysis (KEGG), and other bioinformatics analyses were performed using the OmicStudio tools available at https://www.omicstudio.cn/tool.

Quantitative RT-PCR

Total RNA was isolated from muscle samples using Trizol reagent (Thermo Fisher Scientific, 15596-026). The obtained RNA was reverse transcribed into cDNA using the Reverse Transcription System (Promega, A3500) according to the manufacturer's protocol. Power SYBR® Green RT-PCR reagent kit (Takara, Kyoto, Japan) was used to quantify the PCR amplification products on Lightcycler 480 system (Roche). The primers were detailed in Supplementary Table 2 and normalized to *Gapdh* expression.

Protein extraction and Western blots

Muscle was homogenized in 1x RIPA buffer supplemented with 1 mM PMSF protease inhibitor. BCA assay (ThermoFisher Scientific) was used to estimate protein lysate concentration. Lysates were loaded on a 12–20% SDS-PAGE gel and transferred to nitrocellulose membrane (Merck KGaA, Darmstadt, Germany). Membranes were blotted using antibodies as detailed in Supplementary Table 3. All listed primary antibodies were used at 1:1000, unless noted in the specific legend. And then membranes were washed and incubated with appropriate HRP-conjugated secondary antibodies to develop immunoreactivity (chemiluminescent HRP substrate, MultiSciences), and acquire images using the ChemiDoc Touch Imaging System (BioRad).

Muscle histology

Muscle samples were fixed in 4% paraformaldehyde, embedded in paraffin, sectioned at 5 μm, and stained with hematoxylin and eosin (H&E) after deparaffinization according to standard protocols. For immunostaining of laminin and VDAC1, slides were fixed in 4% paraformaldehyde for 15 min, washed in PBS, incubated in 0.1% Triton X-100 in PBS for 15 min, and then incubated in blocking solution (3% BSA + 5% FBS + 0.1% Tween 20 in PBS) for 1 h at room temperature. The anti- Laminin primary antibodies (1:500, Abcam) or anti-VDAC1 primary antibodies (1:500, Abcam) were incubated at 4 °C overnight. Slides were washed in PBS for 3 times and incubated for 1 h at room temperature with Alexa Fluor secondary antibodies (1:500, goat anti-rabbit, Invitrogen), and sealed with DAPI-containing blocking agent in the end. Images were acquired with Olympus microscopy slideview VS200. Total myofiber number was quantified under consistent aperture and magnification settings, with three random fields of view selected per slide. Researchers using Fiji software to measure 500-800 hundred of myocyte cross-sectional areas (MCSAs) for each mouse under blinded.

Succinate dehydrogenase staining

To visualize the succinate dehydrogenase activity in skeletal muscle, we performed succinate dehydrogenase (SDH) staining. Muscle samples were embedded in tissue freezing media, sectioned at 7 μm and stained with SDH stain kit (Solarbio, G2000) at 37 °C for 15 min. For quantification of SDH staining intensity, 4 images per sample were acquired randomly in the same light intensity and exposure settings using Olympus microscopy slideview VS200. Images were acquired using Zen Pro software and analyzed with Fiji processing software to keep the same threshold.

Immunofluorescence detection of mitochondrial morphology

For immunofluorescence assessment of mitochondrial morphology, frozen cross sections of extensor digitorum longus (EDL) muscles were subjected to staining with antibodies against VDAC1 (ab15895; anti-rabbit; Abcam). Fresh EDL muscles were embedded in optimal cutting temperature compound and cut into 5 μm sections. Slides were fixed in 4% paraformaldehyde for 15 min and permeabilized using 0.1% Triton X-100 for 15 min after 3 washing steps with PBS. Blocking was carried out using 3% BSA + 5% FBS + 0.1% Tween 20 in PBS for 1 h at room temperature. Subsequently, tissue sections were incubated overnight at 4 °C with the VDAC1 antibody (1:500). Following this, slides were washed 3 times with PBS for 10 min each. A fluorescently coupled secondary antibody Alexa Fluor 488 (1:500, goat anti-rabbit, Invitrogen) was applied for 1 h at room temperature. After 3 washing steps with PBS, the slides were sealed with a DAPI-containing blocking agent. Images were acquired using an Olympus confocal microscope (OLYMPUS IX83-FV3000). Standard image processing was performed using Fiji.

Transmission Electron Microscopy (TEM)

For mitochondrial ultrastructure characteristics, TA/GA muscle tissue were cut from the midsection, and the part of red gastrocnemius on the inner side was avoided. These samples were cut into 2 mm^3 cubes (2mmx1mmx1mm) and fixed in 2.5% glutaraldehyde overnight at 4 °C, and then post-fixed with 1% osmium tetroxide for 90 min. Tissues were embedded with epoxypropane resin after dehydration in an ethanol series. Ultrathin sections (~80 nm) were cut with ultra-microtome (Leica EM UC7) and mounted on copper grids with 2% uranyl acetate and 0.2% lead citrate stained. The slices were observed with Tecnai G2 Spirit 120 kV TEM (Thermo FEI) at the Center of Electron Microscopy, Zhejiang University.

Blinded analysis of TEM images

TEM images were analyzed semi-quantitatively using an injury scoring system, evaluated at 5 different locations within each muscle sample. And approximately 20 mitochondria in each field were randomly chosen for analysis. According to mitochondrial ultrastructural characteristics, the severity of ultrastructural injury was assessed by determining a composite score (Scale of 0–5)[62]. Mitochondrial injury score 0 = normal appearance; score 1 = swelling of endoplasmic reticulum or minimal mitochondrial swelling; score 2 = mild mitochondrial swelling; score 3 = moderate or focal high-amplitude swelling; score 4 = diffuse high-amplitude swelling or disruption of cristal membrane integrity; score 5 = high-amplitude swelling with some mitochondrial flocculent densities and/or calcifications. Intermyofibrillar (IMF) mitochondria length and area were evaluated at 5 different locations within each muscle sample. All mitochondria in each field of view were manually measured using Image J.

Treadmill running

We conducted a treadmill running test utilizing a motorized and speed-controlled treadmill system (Columbus Instruments). Before the training, mice underwent a 5-min adaptation on the treadmill at an initial speed of 0 m/min, followed by an additional 5 min at a slow speed of 6 m/min. Throughout the test sessions, the running speed was initiated at 6 m/min and incremented by 3 m/min every 2 min until exhaustion. Mice were considered exhausted if their hindlimbs remained on the electric grid for more than 10 s.

Measurement of muscle strength

Muscle strength was measured using Kondziela's inverted screen test. The mouse was placed in the center of the wire grid system. Then the mouse's head was declining first through rotation the screen to an inverted position over 2 s. The grid-hanging time capacity was calculated by measuring the hanging duration. Alternatively, the grip strength of the forelimb was measured using weights test. 7 weights (20, 33, 46, 59, 72, 85, and 98 g) were set through the apparatus. The mouse was held by the middle of the tail and allowed to grasp the different weights lying on the laboratory table. As its forepaws hold the wire, the mouse was started to raise until clear of the table. If the mouse can hold it for 3 s, it was then changed to the next heaviest weight. If the mouse drops the weight in less than 3 s, the time was recorded at this weight. Detailed procedures and scoring criteria have been reported previously[63].

ATP measurement

Muscle ATP content was quantified utilizing an ATP Assay kit (Beyotime, S0027). In adherence to the manufacturer's guidelines, frozen muscle samples were immersed in 100 μl lysis solution and ground into tissue homogenate. After centrifugation (12,000 g, 4 °C, 5 min), the supernatant was collected and mixed with ATP detection working solution. Then the relative light unit (RLU) value was measured using a luminometer. The lysate concentration was estimated via the BCA assay (ThermoFisher Scientific), and ATP content was expressed in nmol/mg protein.

Statistics and reproducibility

All statistical analyses were performed using IBM SPSS Statistics 24.0 or GraphPad Prism v.8.0. All data were tested for normality distribution. Normally distributed data are presented as mean ± SEM, while non-normally distributed data are presented as median with interquartile range.

Comparisons between two groups were conducted using the unpaired two-tailed Student's t-test or the Mann–Whitney *U*-test. For more than two groups, one-way or two-way ANOVA followed by Sidak's, Games-Howell's, Tukey's multiple comparisons test, or the Kruskal–Wallis with Dunn's multiple comparison test were used. The survival rate was analyzed by Kaplan–Meier analysis and log-rank test. The correlation was analyzed by Pearson correlation coefficient. Each group between 3 and 15 mice for all experiments and the specific number is indicated in the figure legends. All experiments were repeated at least three times. There is a limitation of using small n numbers for RNAseq experiments ($n = 3$ each group).

Reporting summary

Further information on research design is available in the Nature Portfolio Reporting Summary linked to this article.

Data availability

RNA-seq data have been deposited at the Gene Expression Omnibus database with the identifier GSE285318. All data are present in the paper and the supplementary information. The source data behind the graphs in the paper can be found in Supplementary Data.

Received: 29 May 2024; Accepted: 3 February 2025;
Published online: 28 February 2025

References

1. Singer, M. et al. The third international consensus definitions for sepsis and septic shock (Sepsis-3). *JAMA* **315**, 801–810 (2016).
2. Zhu, X. et al. Secreted frizzled-related protein 2 and inflammation-induced skeletal muscle atrophy. *Crit. Care Med.* **45**, e169–e183 (2017).
3. Liu, Y. et al. Gut-muscle axis and sepsis-induced myopathy: the potential role of gut microbiota. *Biomed. Pharmacother.* **163**, 114837 (2023).
4. Prescott, H. C. & Angus, D. C. Enhancing recovery from sepsis: a review. *JAMA* **319**, 62–75 (2018).
5. Evans, L. et al. Surviving sepsis campaign: international guidelines for management of sepsis and septic shock 2021. *Intens. Care Med.* **47**, 1181–1247 (2021).
6. Hyatt, H. W. & Powers, S. K. Mitochondrial dysfunction is a common denominator linking skeletal muscle wasting due to disease, aging, and prolonged inactivity. *Antioxidants***10**, 588 (2021).
7. Owen, A. M. et al. Chronic muscle weakness and mitochondrial dysfunction in the absence of sustained atrophy in a preclinical sepsis model. *Elife* **8**, e49920 (2019).
8. Hood, D. A. et al. Maintenance of skeletal muscle mitochondria in health, exercise, and aging. *Annu. Rev. Physiol.* **81**, 19–41 (2019).
9. Castro-Sepulveda, M. et al. Mitochondria-SR interaction and mitochondrial fusion/fission in the regulation of skeletal muscle metabolism. *Metabolism* **144**, 155578 (2023).
10. Romanello, V. & Sandri, M. Implications of mitochondrial fusion and fission in skeletal muscle mass and health. *Semin. Cell Dev. Biol.* **143**, 46–53 (2022).
11. Fealy, C. E. et al. Skeletal muscle mitochondrial network dynamics in metabolic disorders and aging. *Trends Mol. Med.* **27**, 1033–1044 (2021).
12. Kamerkar, S. C. et al. Dynamin-related protein 1 has membrane constricting and severing abilities sufficient for mitochondrial and peroxisomal fission. *Nat. Commun.* **9**, 5239 (2018).
13. Hong, X. et al. Mitochondrial dynamics maintain muscle stem cell regenerative competence throughout adult life by regulating metabolism and mitophagy. *Cell Stem Cell* **29**, 1298–1314.e10 (2022).
14. Favaro, G. et al. DRP1-mediated mitochondrial shape controls calcium homeostasis and muscle mass. *Nat. Commun.* **10**, 2576 (2019).
15. Mankowski, R. T. et al. Pathophysiology and treatment strategies of acute myopathy and muscle wasting after sepsis. *J. Clin. Med.* **10**, 1874 (2021).
16. Ferrucci, L. & Fabbri, E. Inflammageing: chronic inflammation in ageing, cardiovascular disease, and frailty. *Nat. Rev. Cardiol.* **15**, 505–522 (2018).
17. Callahan, L. A & Supinski, G. S Sepsis-induced myopathy. *Crit., Care Med*. **37**, S354–S367 (2009).
18. Zanders, L. et al. Sepsis induces interleukin 6, gp130/JAK2/STAT3, and muscle wasting. *J. Cachexia Sarcopenia Muscle* **13**, 713–727 (2022).
19. Eggelbusch, M. et al. The NLRP3 inflammasome contributes to inflammation-induced morphological and metabolic alterations in skeletal muscle. *J. Cachexia, Sarcopenia Muscle* **13**, 3048–3061 (2022).
20. Hahn, A. et al. Serum amyloid A1 mediates myotube atrophy via Toll-like receptors. *J. Cachexia Sarcopenia Muscle* **11**, 103–119 (2020).
21. Cohen, S., Nathan, J. A. & Goldberg, A. L. Muscle wasting in disease: molecular mechanisms and promising therapies. *Nat. Rev. Drug Discov.* **14**, 58–74 (2015).
22. Kraakman, M. J. et al. Neutrophil-derived S100 calcium-binding proteins A8/A9 promote reticulated thrombocytosis and atherogenesis in diabetes. *J. Clin. Investig.* **127**, 2133–2147 (2017).
23. Akira, S. et al. Identification of hHuman S100A9 as a novel target for treatment of autoimmune disease via binding to Quinoline-3-Carboxamides. *PLoS Biol.* **7**, e97 (2009).
24. Cox, M. C. et al. The impact of sarcopenia and acute muscle mass loss on long-term outcomes in critically ill patients with intra-abdominal sepsis. *J. Cachexia Sarcopenia Muscle* **12**, 1203–1213 (2021).
25. Zheng, Y. et al. Endoplasmic reticulum stress promotes sepsis-induced muscle atrophy via activation of STAT3 and Smad3. *J. Cell Physiol.* **238**, 582–596 (2023).
26. Casas-Martinez, J. C., Samali, A. & McDonagh, B. Redox regulation of UPR signalling and mitochondrial ER contact sites. *Cell Mol. Life Sci.* **81**, 250 (2024).
27. Willemen, H. L. D. M. et al. Inflammation-induced mitochondrial and metabolic disturbances in sensory neurons control the switch from acute to chronic pain. *Cell Rep. Med.* **4**, 101265 (2023).
28. Wang, S. et al. S100A8/A9 in Inflammation. *Front. Immunol*. **9**, 1298 (2018).
29. Jakobsson, G. et al. Therapeutic S100A8/A9 blockade inhibits myocardial and systemic inflammation and mitigates sepsis-induced myocardial dysfunction. *Crit. Care* **27**, 374 (2023).
30. Boyd, J. H. et al. S100A8 and S100A9 mediate endotoxin-induced cardiomyocyte dysfunction via the receptor for advanced glycation end products. *Circ. Res*. **102**, 1239–1246 (2008).
31. Li, Y. et al. S100a8/a9 signaling causes mitochondrial dysfunction and cardiomyocyte death in response to ischemic/reperfusion injury. *Circulation* **140**, 751–764 (2019).
32. Cho, D. S. et al. Single-cell deconstruction of post-sepsis skeletal muscle and adipose tissue microenvironments. *J. Cachexia Sarcopenia Muscle* **11**, 1351–1363 (2020).
33. Zhang, Y. et al. Deficiency of S100A9 alleviates sepsis-induced acute liver injury through regulating AKT-AMPK-dependent mitochondrial energy metabolism. *Int. J. Mol. Sci.* **24**, 2112 (2023).
34. Wu, F. et al. S100a8/a9 contributes to sepsis-induced cardiomyopathy by activating ERK1/2-Drp1-mediated mitochondrial fission and respiratory dysfunction. *Int. Immunopharmacol.* **115**, 109716 (2023).
35. Shi, W. et al. Blockage of S100A8/A9 ameliorates septic nephropathy in mice. *Front. Pharmacol.* **14**, 1172356 (2023).
36. Gonzalez, L. L., Garrie, K. & Turner, M. D Role of S100 proteins in health and disease. *Biochim. Biophys. Acta Mol. Cell Res.* **1867**, 118677 (2020).
37. Zink, W. et al. Alterations in intracellular Ca2+-homeostasis of skeletal muscle fibers during sepsis. *Crit. Care Med.* **36**, 1559–1563 (2008).
38. Daussin, F. N., Boulanger, E. & Lancel, S. From mitochondria to sarcopenia: role of inflammaging and RAGE-ligand axis implication. *Exp. Gerontol.* **146**, 111247 (2021).
39. Riuzzi, F. et al. RAGE in the pathophysiology of skeletal muscle. *J. Cachexia Sarcopenia Muscle* **9**, 1213–1234 (2018).

40. Chiappalupi, S. et al. Targeting RAGE prevents muscle wasting and prolongs survival in cancer cachexia. *J. Cachexia Sarcopenia Muscle* **11**, 929–946 (2020).
41. Chiu, C. Y. et al. Advanced glycation end-products induce skeletal muscle atrophy and dysfunction in diabetic mice via a RAGE-mediated, AMPK-down-regulated, Akt pathway. *J. Pathol.* **238**, 470–482 (2016).
42. Su, S.-C. et al. Cilostazol inhibits hyperglucose-induced vascular smooth muscle cell dysfunction by modulating the RAGE/ERK/NF-κB signaling pathways. *J. Biomed. Sci.* **26**, 1–13 (2019).
43. Mao, Y. X. et al. RAGE-dependent mitochondria pathway: a novel target of silibinin against apoptosis of osteoblastic cells induced by advanced glycation end products. *Cell Death Dis.* **9**, 674 (2018).
44. Huang, C. Y. et al. HMGB1 promotes ERK-mediated mitochondrial Drp1 phosphorylation for chemoresistance through RAGE in colorectal cancer. *Cell Death Dis.* **9**, 1004 (2018).
45. Kraus, F. et al. Function and regulation of the divisome for mitochondrial fission. *Nature* **590**, 57–66 (2021).
46. Romanello, V. & Sandri, M. The connection between the dynamic remodeling of the mitochondrial network and the regulation of muscle mass. *Cell. Mol. Life Sci.* **78**, 1305–1328 (2020).
47. Touvier, T. et al. Muscle-specific Drp1 overexpression impairs skeletal muscle growth via translational attenuation. *Cell Death Dis.* **6**, e1663 (2015).
48. Romanello, V. et al. Mitochondrial fission and remodelling contributes to muscle atrophy. *EMBO J.* **29**, 1774–1785 (2010).
49. Mao, X. et al. Phosphorylation of Dynamin-Related Protein 1 (DRP1) regulates mitochondrial dynamics and skeletal muscle wasting in cancer cachexia. *Front. Cell Dev. Biol.* **9**, 673618 (2021).
50. Rexius-Hall, M. L. et al. Mitochondrial division inhibitor 1 (mdivi-1) increases oxidative capacity and contractile stress generated by engineered skeletal muscle. *FASEB J.* **34**, 11562–11576 (2020).
51. Lee, H. et al. Mitochondrial dysfunction in skeletal muscle contributes to the development of acute insulin resistance in mice. *J. Cachexia Sarcopenia Muscle* **12**, 1925–1939 (2021).
52. Zeng, X. et al. Activated Drp1 regulates p62-mediated autophagic flux and aggravates inflammation in cerebral ischemia-reperfusion via the ROS-RIP1/RIP3-exosome axis. *Mil. Med. Res.* **9**, 25 (2022).
53. Boutin, R. D. et al. Sarcopenia: current concepts and imaging implications. *AJR Am. J. Roentgenol.* **205**, W255–W266 (2015).
54. Xia, J. et al. RAGE is a receptor for SARS-CoV-2 N protein and mediates N Protein–induced Acute Lung Injury. *Am. J. Respir. Cell Mol. Biol.* **69**, 508–520 (2023).
55. He, X. et al. BAY61-3606 attenuates neuroinflammation and neurofunctional damage by inhibiting microglial Mincle/Syk signaling response after traumatic brain injury. *Int. J. Mol. Med.* **49**, 1–13 (2022).
56. Chen, S. N. et al. Deletion of TLR4 attenuates lipopolysaccharide-induced acute liver injury by inhibiting inflammation and apoptosis. *Acta Pharm. Sin.* **42**, 1610–1619 (2021).
57. Cao, P. et al. Early-life inflammation promotes depressive symptoms in adolescence via microglial engulfment of dendritic spines. *Neuron* **109**, 2573–2589.e9 (2021).
58. Hou, L. et al. Nontoxic concentration of ochratoxin A decreases the dosage of cyclosporine A to induce chronic nephropathy model via autophagy mediated by toll-like receptor 4. *Cell Death Dis.* **11**, 153 (2020).
59. Rittirsch, D. et al. Immunodesign of experimental sepsis by cecal ligation and puncture. *Nat. Protoc.* **4**, 31–36 (2009).
60. Schmidt, F. et al. The E3 ubiquitin ligase TRIM62 and inflammationinduced skeletal muscle atrophy. *Crit. Care* **18**, 545 (2014).
61. Yang, B. et al. IL-6 deficiency attenuates skeletal muscle atrophy by inhibiting mitochondrial ROS production through the upregulation of PGC-1α in Septic Mice. *Oxid. Med. Cell. Longev.* **27**, 9148246 (2022).
62. Crouser, E. D. et al. Endotoxin-induced ileal mucosal injury and nitric oxide dysregulation are temporally dissociated. *Am. J. Respir. Crit. Care Med.* **161**, 1705–1712 (2000).
63. Deacon, R. M. Measuring the strength of mice. *J. Vis. Exp.* **76**, 2610 (2013).

Acknowledgements

We would like to express our sincere gratitude to Jinchao Hou for her valuable discussions and Xiangyang Yu for his assistance with the clinical specimens for this study. This research was supported by the National Natural Science Foundation of China (82230074 to X.F., 82072221 to K.Z. and 82302425 to H.Y.), Youth Science Foundation of Guangxi Medical University (GXMUYSF202306 to D.H.), and Youth Program of Scientific Research Foundation of Guangxi Medical University Cancer Hospital (YQJ2022-1 to D.H.). Graphical Abstract was modified from Servier Medical Art (https://smart.servier.com/), licensed under a Creative Commons Attribution 4.0 Generic License. (https://creativecommons.org/licenses/by/4.0/). Figures 4a and 7a were created with BioRender (https://www.biorender.com/), and we have provided the image license in the supplementary materials.

Author contributions

D.H., K.Z., and X.F. conceptualized and designed the project. D.H., Y.L., Y.G., and Y.Z. performed the experiments. Y.G. and M.W. contributed to clinical sample collection and analysis. Y.L., H.Y., and D.H. conducted statistical analysis of the data. X.F., K.Z., and D.H. obtained the data and wrote the manuscript. F.L. and K.Z. provided constructive comments and intellectual discussion. X.F. and K.Z. supervised the study. All authors contributed to the article and approved the final version of the manuscript.

Competing interests

The authors declare no competing interests.

Additional information

Supplementary information The online version contains supplementary material available at https://doi.org/10.1038/s42003-025-07654-3.

Correspondence and requests for materials should be addressed to Kai Zhang or Xiangming Fang.

Peer review information *Communications Biology* thanks Jacob Brown, Mark Burton and the other, anonymous, reviewer(s) for their contribution to the peer review of this work. Primary Handling Editors: Jesmond Dalli and Dario Ummarino.